# Surface-Treated Nanofibers as High Current Yielding Breath Humidity Sensors for Wearable Electronics

Sathvik Ajay Iyengar,[†] Pillalamarri Srikrishnarka,[†,‡] Sourav Kanti Jana,[†] Md Rabiul Islam,[†] Tripti Ahuja,[†] Jyoti Sarita Mohanty,[†] and Thalappil Pradeep*,[†]

[†]DST Unit of Nanoscience, Thematic Unit of Excellence, Department of Chemistry, and [‡]Department of Chemical Engineering, Indian Institute of Technology Madras, Chennai 600036, India

S Supporting Information
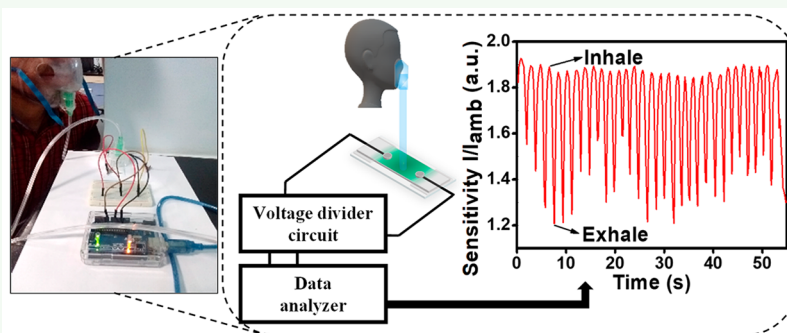
ABSTRACT: As wearable electronics have gained momentum in the past few years, there is a dire need for smart, responsive, and, most importantly, affordable sensors for biological monitoring. One such noninvasive method to gauge body metabolism is via breath analysis. In a successful attempt to sense and record relative humidity levels (%RH) in nasal and oral breath, this work presents an economical route to fabricate a wearable humidity sensor with high sensitivity and a response time of ~1 s. The sensor consists of a flexible backbone of electrospun poly(vinylidene fluoride)/reduced graphene oxide (PVDF/rGO) nanofibers which have been selectively sensitized to humidity via surface polymerization of aniline using the inexpensive successive ionic layer adsorption and reaction (SILAR) technique. We report a high sensitivity and a full response range (0− 95% RH) supported by a low working voltage and minimalistic circuitry as an attractive feature for integration into wearable electronics. Moreover, as the device sensitivity is adequate even up to 95% RH, it is conducive to detect nasal breath and saturated humidity conditions accurately. As the method utilizes electrospinning, this work involves the preparation of such humidity sensors on a large scale (up to 400 units using 8 mg of rGO) with the benefit of having affordable and cost-effective devices.

KEYWORDS: humidity sensing, reduced graphene oxide, nanofibers, polyaniline, SILAR

INTRODUCTION

Measurement of humidity is important from several perspectives. Industries such as that of electronics, food, medicine, materials, and metallurgy are concerned about varying humidity levels.[1−4] Relative humidity levels also have a significant impact on the survival rates of airborne infectious agents[5−7] and hence need to be monitored and controlled accordingly. On the other end of the spectrum, humidity levels in exhaled breath is a reliable marker of the quality of body metabolism and health.[8,9] Although it can be controlled, breath rate is almost always synchronous with heart rate. Hence, a subject's breath rate, tidal volumes, and exhaled air quality can be tied to various parameters such as their age, quality of living, and even heart rate and its condition.[10] This rich collection of data obtained in a noninvasive manner paves the way to monitor various hidden symptoms and diagnose conditions much before they manifest physically. For a technology of this kind to be available across the world, it must be sensitive and

selective with fast response time while, most importantly, being affordable. We demonstrate a methodology for making this possible.

Electrospinning is a simple, yet powerful tool for obtaining nanofibers which are used in many applications, varying from water purification and air filtration to production of anodic materials in solar cells and in batteries and capacitors.[11−14] Briefly, it is a technique wherein a high electrical potential is applied between a droplet and a collector plate, and as a result, the voltage overcomes the surface tension at the solution−air interface and causes the liquid droplet to change its shape to form a cone. The droplet then elongates, followed by continuous "drawing", leading to the formation of nanofibers. Electrospun fibers with hierarchical structures of one or many
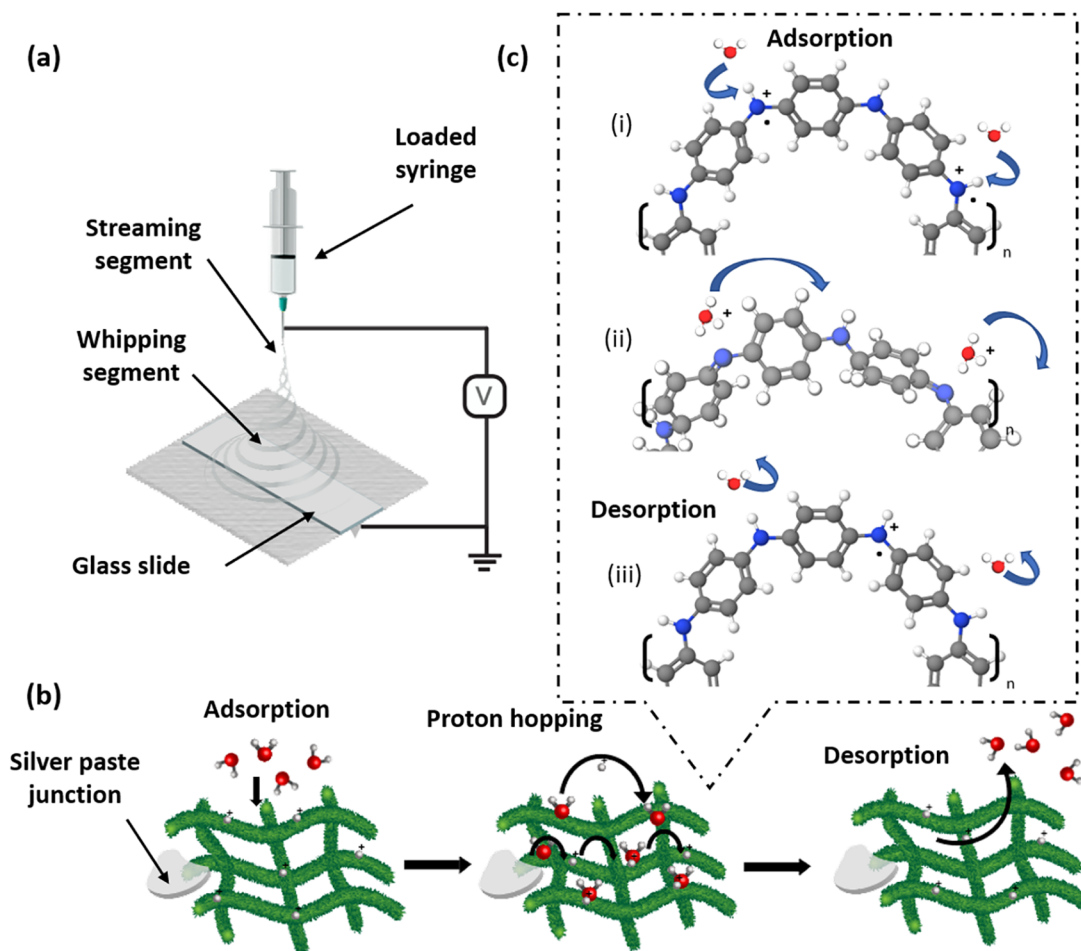
Figure 1. (a) Schematic showing electrospinning setup. (b) Zoomed-in schematic, elaborating the sensing process at the electrode junction. (c) Grotthuss mechanism of proton hopping: (i) adsorption of H_2O onto PANi ES backbone; (ii) proton transfer from partly protonated PANi backbone to H_2O, where (iii) proton hops from H_3O^+ species to PANi ES.

constituents can be obtained by this technique. This process yields robust fibers, which can be replicated easily in large-scale once parameters such as flow rate, working voltage, sample distance, and number of revolutions of the collecting surface are optimized. In this work, we have prepared a poly-(vinylidene difluoride) (PVDF) nanofiber backbone via electrospinning as it has been proven to be a durable and flexible substrate material for wearable electronics.[15] We have used the successive ionic layer adsorption reaction (SILAR) or the successive ionic layer deposition (SILD) as a cost-effective, simple, and versatile technique for obtaining thin film coating on PVDF fibers. This method was first introduced by Nicolau in the mid-1980s and has been used for the growth of quantum dots (QDs) such as CdSe, ZnS, and CdTe[16] for the fabrication of nanocrystal films[17] and gas sensors.[18,19] It is a highly versatile procedure involving the immersion of a substrate separately in two different precursor solutions and washing in water after each immersion to remove weakly bound species. Thus, one SILAR cycle consists of adsorption of the cation precursor, rinsing with water, and adsorption of the anion precursor, followed by a chemical reaction and another rinsing, in the process of synthesizing the above quantum dots. This self-limiting procedure gives good control of the layer growth. When these cycles are performed in succession, we observe the growth of a thin layer of the desired material.

Polyaniline (PANi) has been used for decades due to its versatility as a conducting polymer. Although other conducting polymers such as polypyrrole and porphyrin complexes have been used as sensors,[20−25] the reliability, stability, and hydrophilicity of PANi[26,27] combined with the sturdy backbone[28−30] and biocompatibility of PVDF[31−33] makes it conducive to prepare a sensing element tailored toward atmospheric and breath moisture. Previous reports of metal oxide nanostructures, graphene, and other active materials in humidity sensors indicate a response in the nanoamperes range, warranting expensive device fabrication, rectification, and amplification circuitry and energy-intensive methodologies.[34−39] Primary assembly of the sensor requires multiple steps starting from the preparation of metal oxide nanostructures, heat treatment to obtain the required phase, and finally the assembly of the electrode.[40]

Many reports on breath humidity sensors present faster response and good sensitivity, but these methods face economic challenges due to their complexity in the process of upscaling for mass production.[41−43] The use of common materials and room temperature operation conditions with fast response time of ∼1 s makes our material ideal for breath monitoring.[44,45] We further enhanced the performance by incorporating rGO in the electrospun fibers. There have been reports of improved conductance when rGO is introduced into a polymer matrix[46,47] Also, in contrast to recent reports,[48] our

sensor uses minimal circuitry, and the material is optimized to be cost-effective. We have demonstrated a stark and previously unreported difference in nasal and oral breath humidity and breath patterns and established the advantage of increased sensitivity at higher RH levels.

■ EXPERIMENTAL SECTION

Detailed experimental conditions for synthesizing rGO can be found elsewhere (see the Supporting Information).

Preparation of Nanofiber Backbone. PVDF (3.29 g) was dissolved in DMF (13 mL) and stirred for 3 h until homogeneity was obtained. Simultaneously, rGO (8 mg) was ultrasonicated in DMF (2 mL) for 30 min to obtain a uniform dispersion. This dispersion of rGO was subsequently added to the stirring solution of DMF to result in an 18 wt % PVDF solution in DMF. The final electrospinning solution was left to stir further for 6 h under ambient temperature. Nanofibers were prepared by using the ESPIN-NANO electrospinning machine by loading the e-spin solution into a 2 mL capacity syringe. Spinning parameters were set to a flow rate of 2 mL h^{-1}, a working distance of 13 cm, and a voltage of 13 kV for a period of 1 h. These PVDF/rGO nanofibers were thus spun onto a series of glass slides as shown in Figure 1a.

Surface Polymerization of Aniline on the Nanofibers. Aniline (1 mL) [A] and APS (1.45 g) [B] were added separately to two beakers, each containing preprepared 1 M aqueous HCl (40 mL) solution. The electrospun fiber mat was then taped to the supporting glass slide to fix it in position. SILAR was then performed by alternatingly dipping and withdrawing the glass slides between solutions A and B. The dwell period was 3 min in solution A and 2 min in solution B. After each cycle, the slides were washed in deionized water to remove excess reactants. This was performed for 10 cycles, and the color change of the slides indicated the polymerization of aniline to PANi-emeraldine base (EB) and its phase change to the more conducting emeraldine salt (ES) form by the acid doping process. Finally, the chemically treated fibers were left to dry under ambient conditions for 2 h.

Other experimental details and characterization techniques are presented in the Supporting Information.

■ RESULTS AND DISCUSSION

Synthesis of Nanofibers and Imaging by Scanning Electron Microscopy (SEM). Electrospinning was used to fabricate the humidity sensor, wherein PVDF/rGO in DMF was electrospun under a voltage of 13 kV and a flow rate of 2 mL h^{-1} as previously discussed in the Experimental Section. A schematic representation of the SILAR protocol for deposition of PANi on the PVDF fibers is shown in Figure 2a. The initial diameter distribution of the fibers and their surface morphology are shown in the SEM micrograph shown in Figure 2b. The fibers had a smooth surface, without any discontinuities. Figure 2c presents an even deposition of PANi on the fiber surface after SILAR, which explains the lateral widening of the fibers. The surface morphology has now been altered to attain a rough exterior, which is believed to aid in the adsorption−desorption process. The fiber diameters of the bare electrospun fibers were in the range 200−380 nm before and 525−550 nm after SILAR, with an average fiber diameter of 255 and 528 nm, respectively, as given in Figure 2d. Conventionally, the width of the fibers has been represented as the diameter of the fibers.

Raman Spectral Analysis of Nanofibers. To confirm the presence of PVDF and rGO, Raman spectra were collected as shown in Figure S1a. Solutions of PVDF and PVDF-rGO were drop-casted separately onto microscope slides and were left to dry. Once dried, the spots were viewed under a Raman microscope. The peaks present at 790 and 886 cm^{-1} confirm
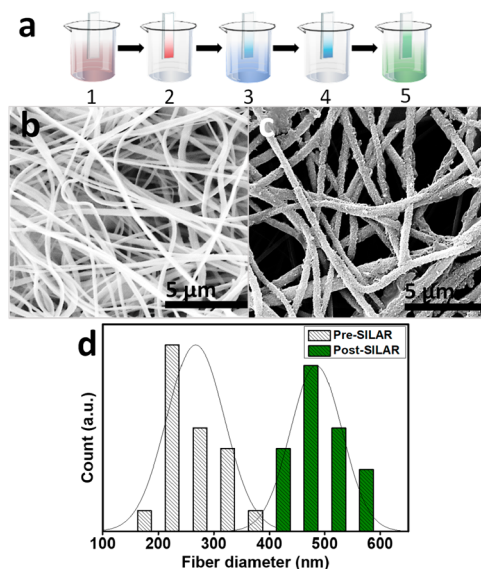
Figure 2. (a) Steps performed to surface polymerize aniline via SILAR: (1) PVDF/rGO fibers immersed in 0.28 mM aqueous solution of A, (2) fibers immersed in water to remove excess A, (3) fibers immersed in 0.15 mM aqueous solution of APS to initiate the polymerization, (4) fibers in water to remove the unreacted APS, and (5) PANi EB doped to ES. SEM of PVDF/rGO nanofibers (b) before SILAR treatment, (c) after SILAR treatment, and (d) diameter distribution extracted from the images.

the presence of α and β phases of PVDF, respectively. The ratio of their intensities indicates the predominance of the α phase, which was observed in commercial grade PVDF.[53] The peaks at 1345 and 1595 cm^{-1} in PVDF-rGO blend indicate the D and G bands of rGO. To confirm the formation of rGO, the prepared sample was drop-casted onto microscopic glass slides, and Raman spectra were collected as shown in Figure S1a. The corresponding D, G 2D, and D+G bands of rGO have been indicated. The PANi-treated electrospun fiber mat was placed under a 20× objective of the Raman microscope for collecting the time lapse spectra. Initially, the sensor was saturated with humidity by continuous oral exhalation before placing it under the microscope. The Raman spectra with saturated humidity are shown in Figure S1b. Also, the peak at 831 cm^{-1} corresponds to the β phase of PVDF, and the absence of a peak at 790 cm^{-1} suggests the complete conversion of the α phase to β phase of PVDF, which possibly occurs during electrospinning.[54] A high voltage of 20 MV/m is usually applied for the phase transformation of α to β due to the dipolar arrangement.[55] The peaks at 1174 and 1344 cm^{-1} are assigned to the δ(CH) in-plane bending and ν(C−N$^+$) stretching, respectively. The peak at 1507 cm^{-1} corresponds to the δ(NH) bending, and the peaks in the 1660−1645 cm^{-1} have been attributed to substituted phenazine[56] structures. This is understood to be crucial in the formation of the 2D polymer framework. The broad peak at 3000 cm^{-1} is attributed to the grouped stretching frequencies of C−H and N−H stretching at 3300 cm^{-1}.[57] The hydrogen bond present in water holds a key role in many biological and chemical processes. This can be studied by monitoring the OH stretching frequencies.[58] As water molecules have a tendency to form water clusters, the hydrogen bonding in water cluster could be classified into proton donor (PD) or proton acceptor (PA). A strong peak around 3002 cm^{-1} corresponds to the strongest hydrogen-bound OH for a single donor−double
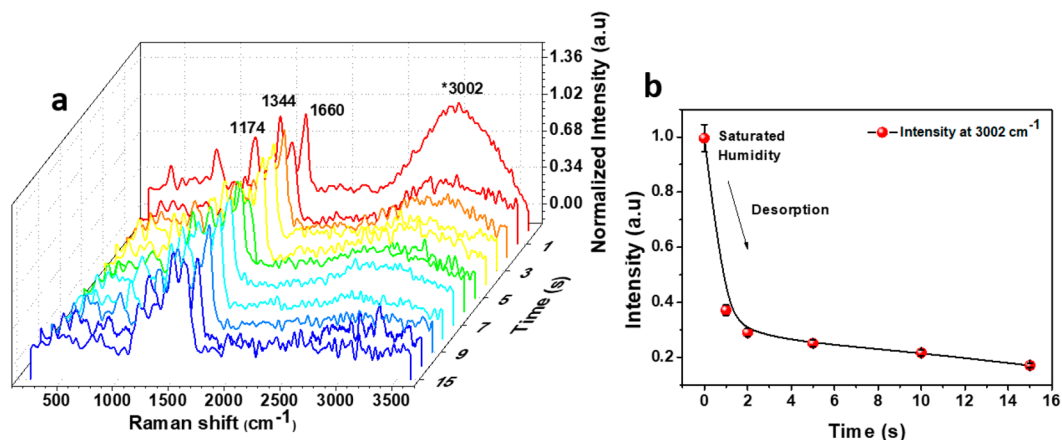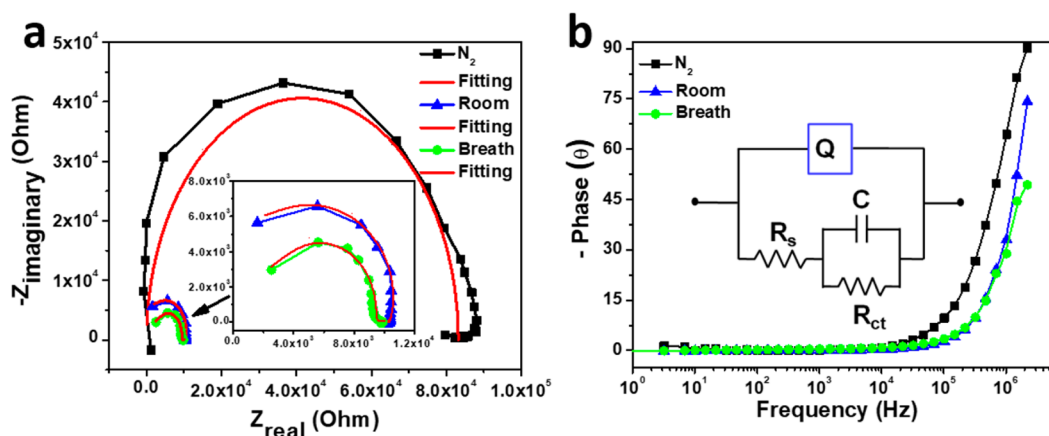
Figure 3. (a) Real-time Raman spectroscopy indicating desorption of water. (b) Variation of the 3002 cm^{-1} peaks with time.

| Parameter	N$_2$ gas	Room conditions	Breath
Q [F.s$^{(a-1)]}$]	8.6×10^{-12}	3.8×10^{-12}	8.3×10^{-12}
a	1	0.9	0.9
R$_{ct}$ [KΩ]	82.9	10.8	9.5
R$_s$ [KΩ]	2.4	0.208	0.347
C [F]	73×10^{-7}	2.3×10^{-7}	0.5×10^{-7}

Figure 4. (a) Nyquist plot to determine the R_s and R_{ct} of the sensor under room (RH = 44%) and nasal breath (RH = 88%) conditions and under N$_2$ (absence of humidity RH = 0%). (b) Bode plot of the sensor to understand the phase of C capacitance. Inset: circuit arrangement used for fitting the Nyquist plot. (c) Capacitive and resistive parameters for the setup constant phase element (CPE) under various humidity conditions.

acceptor cluster.[59] We suggest that there could be a hydrogen bond between the $-(NH)^+-$ of PANi and H$_2$O as it is necessary for proton hopping. The peaks at 1344 and 3002 cm^{-1} support the adsorption and proton hopping mechanism. The decrease in the intensity might be due to the loss in hydrogen bonding as water desorbed. Time lapse Raman spectra were collected for a total duration of 15 s in which the decrease in the intensity of the peak at 3002 cm^{-1} was observed (Figure 3a). This change is graphically shown in Figure 3b. The intensity decreased by~ 66% within 1 s upon exposure to humidity. However, for a complete decrease in the peak intensity it took ~16 s. The prevailing temperature and % RH during the time of collecting the spectra were 20 °C and

50% RH, respectively. The low temperature during testing made it convenient to capture the entire sorption over time.

IR/ATR Spectral Analysis of Nanofibers. IR spectral data were obtained for the nanofiber sample before and after SILAR treatment to confirm the presence of PANi as shown in Figure S2. The peak at 1400 cm^{-1} observed in both the samples can be assigned to C−F stretching. The peaks at 1065 and 880 cm^{-1} indicate C=C trans-conformer of vinylidene and C−C−C asymmetrical stretching modes,[51] respectively. The characteristic peaks at 1566 and 2115 cm^{-1} correspond to the N−H and the C=N stretching frequencies which are not visible in the PVDF/rGO sample. The C−N bond appears at 1299 cm^{-1}. The presence of both C−N and C=N is a hallmark of PANi in the emeraldine base form as its polymeric backbone is
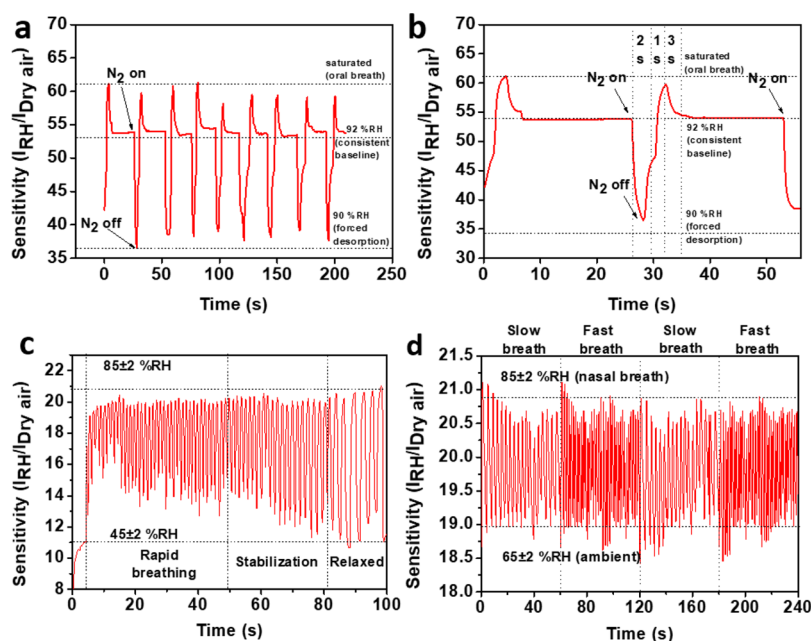
Figure 5. Chronoamperometric studies highlighting differences between (a) sensor response to nasal breath immediately after 15 min of moderate cardio exercise and (b) sensor response to alternating slow and fast nasal breath cycles (manually induced). (c, d) Testing the sensitivity at nearly saturated humidity levels caused by oral exhalation.

partly protonated. The broad peak at 2690 cm^{-1} can be attributed to the intermolecular N−H stretch which is evident only in the PANi-coated fibers, indicating adsorption of atmospheric moisture post SILAR treatment. Additionally, an out-of-plane (oop) N−H bend was visualized at 800 cm.$^{-1}$ The weak signal at 1995 cm^{-1} suggests the presence of a ketenimine C═C═N group.[52] All of these correspond to the PVDF backbone and the emeraldine structure of PANi.

TEM Analysis of RGO and PVDF/RGO Nanofiber. TEM micrographs of the as-prepared rGO and PVDF/rGO nanofiber are shown in Figure S3. Figure S3a shows a low-magnification TEM image of rGO. A single sheet is transparent to the electron beam, wrinkled, and also folded at the edges. The corresponding image in the inset shows a high-magnification TEM image of rGO; the transparency and wrinkles are evident. A low-magnification TEM of PVDF/rGO nanofiber is shown in Figure S3b; the fiber diameter from this image does match the fiber diameter from the SEM. A high-magnification TEM image of a nanofiber is shown in Figure S3c,d. We observe the rGO flake protruding out from the PVDF fiber. Because of the low concentration of rGO (8 mg), we do not observe a uniform covering of rGO on the PVDF fiber.

PANi Phase Characterization by Cyclic Voltammetry (CV). To phase characterize the PANi that was coated on the fibers, PANi was coated on indium-doped tin oxide (ITO)-coated glass via SILAR. This glass slide was subjected to cyclic voltammetry using 0.5 M H_2SO_4 as electrolyte, at a scan rate of 50 mV s^{-1} and cycled between 0.4 and 0.8 V. The corresponding CV is shown in Figure S4; the corresponding voltammogram has two peaks at 0.7 and −0.2 V. The broad peaks could be due to nonuniform coating of PANi on ITO. Upon coating of PANi on ITO, a slight greenish coloration was observed on ITO glass, which confirmed the coating. The presence of a peak at 0.7 V confirms the presence of PANi in the emeraldine salt form.[49,50]

Contact Angle Measurements. Optical images obtained during contact angle measurements for the nanofiber sample before and after PANi coating via SILAR are presented in Figures S8a and S8b, respectively. The corresponding contact angles were 125° and 76° without and with PANi coating. This confirms the change in physical affinity toward moisture from a hydrophobic backbone surface to a hydrophilic one.

Impedance Measurements and Studies. Impedance spectroscopy was conducted to investigate the conduction mechanism of humidity sensing, and results are shown in Figure 4a−c. A complex impedance spectrum was measured by applying an ac signal (20 mV) along with a dc voltage (2 V) between two silver metallic contacts formed on the PANi-coated nanofibers. The frequency of the ac signal was varied from 7 MHz to 10 Hz, and the subsequent change of impedance was recorded as a function of frequency. This sets up a constant phase element (CPE). Figure 4a shows the Nyquist plot which describes the charge transfer resistance between two electrodes in the absence/presence of humidity. Because of the adsorption of N_2 gas onto the fiber mat, a double-layer capacitor is formed. This is attributed to high charge transfer resistance (R_{ct}) as well high surface capacitance (C) of the mat. Figure 4c displays these parameters along with the parameters Q and a which appear in the constant phase element's impedance equations. However, under room conditions (25 °C, RH ∼ 44%) and humid conditions (RH ∼ 88%), R_{ct} was reduced drastically in the presence of exhaled nasal breath. The capacitance C in the absence of humidity was 73 × 10^{-7} F, and this decreased drastically in the presence of humidity. We attribute R_s to the surface resistance of PANi fibers and R_{ct} to the resistance associated with proton hopping due to the aforementioned changes. In the presence of humidity, water molecules were adsorbed onto the electrode surface and formed an electrical double layer containing OH$^-$. The change in phase angle (Bode plot) as a function of frequency has been depicted in Figure 4b. Under N_2 gas, the phase angle was found to be 90° at higher frequencies (close to
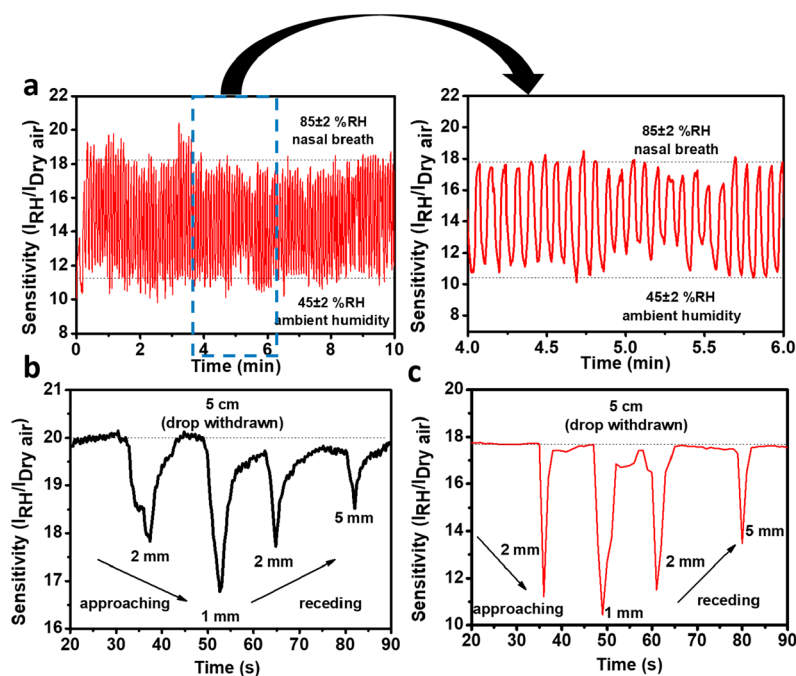
Figure 6. (a) Chronoamperometric studies of nasal breath indicating sensor's signal stability and response. Proximity drop test conducted for pure (b) acetone and (c) ethanol. In (b) and (c), the drop was shifted toward and then away from the sensor element. Sensor response was captured at the various elevations mentioned above.

7 MHz) and nearly zero at lower frequencies, exhibiting the capacitive nature of the material. Whereas, in humid conditions, the phase angle decreased, attributing to the resistive behavior of the active surface of the material. Thus, the sensing mechanism is mostly influenced by a change in resistance of the material in the presence of humidity. The sensor response is presented in terms of sensitivity, where sensitivity is obtained by dividing the I_{RH} with $I_{Dry\,air}$. Here, I_{RH} represents the current value obtained at that particular %RH, and $I_{Dry\,air}$ represents the current value obtained by the sensor in the presence of pure N_2 gas.

Oral Breath Analysis. Chronoamperometric testing was performed initially by alternating between three levels of relative humidity (%RH) to observe the response current range and response time hysteresis. Although oral breath presents a near humidity saturation, on shorter bursts, we achieved sensor response even at levels >90% RH. After each oral exhalation, the calibrated response measured at >95%. The sensor was then left undisturbed for desorption to occur. Although not complete due to possible saturation effects, the desorption occurred consistently to reach 92% RH in 3 s, which was subsequently marked as our baseline. Diffusing N_2 gas onto the sensor surface caused a forced desorption to reach 90% RH. The response time was inversely proportional to the change in %RH exposure; i.e., sorption kinetics was faster when alternating between the "consistent baseline" (92% RH) and "oral breath"(>95% RH) when compared to switching between "forced desorption" (90% RH) and "consistent baseline" (92% RH) as shown in Figure 5a,b. Through these repeated cycles of switching, we were able to establish a full range of sensitivity toward humidity, specifically from 90% RH to saturation. Peng et al. fabricated a breath sensor for obtaining a static response from breath in the offline mode and analyzed it for detecting lung cancer.[60] We propose a real-time operating sensor relying on the continuous breath in contrast to static analysis. Hence, this range is highly crucial in

determining various health aspects tied to the breath rate. Furthermore, conducting oral breath measurements in addition to controlled humidity calibration experiments is crucial to establish the utility of the sensing element under exaggerated humidity and dynamic breath conditions. Experiments involving controlled humidity calibration can be found elsewhere (see Figure S5).

Nasal Breath for Health Monitoring. As the sensor setup was shown to provide quick and crisp data from breath tests, further examinations were conducted to verify its flexibility for health monitoring. Data were collected after 15 min of moderate cardiovascular exercise to study the changes in breath responses and are presented in Figure 5c. Sensor characteristics reveal a very clear demarcation of three stages of breathing post workout. Starting with the initial stage of rapid breathing, which is found to be at 56 breaths/min for a period of 45 s, a gradual decrease in breath rate as well as humidity saturation was observed. This decrease was attributed to a period of breath stabilization, lasting for around 15 s. Finally, the volunteer's breath rate returned to normal breathing as seen evidently. A blank was also conducted by manually alternating between fast and slow breath cycles and is presented in Figure 5d. Thus, a clear difference is observed between natural and artificially simulated breath cycles. This distinguishing ability is essential "smart" feature for wearable electronics. An image of the final setup layout during breath sensing is shown in Figure S7b. As the sensor responds appropriately to breath rate and regularity, it may find applications in various fields such as interrogation and polygraph testing.[61]

Sensor Response and Material Stability. Additional tests were performed to confirm sensor response and stability over time. Sensor data were collected for a longer duration of ~10 min of continuous monitoring as shown in Figure 6a. An expanded view of this data is shown in Figure 6a (right); the response between 4 and 6 min shows a consistent response in

current. The sensor was subjected to continuous breathing cycles for a period of 10 min during which the volunteer was relaxed. Data collected conformed to a fixed response range, indicating no drastic or sudden changes. Although minor variations were detected and can be attributed to the uniqueness of each breath cycle, this does not affect the breath rate and humidity levels visualized. The SILAR-treated nanofiber mat had been stored in atmospheric conditions for a period of 1 week before this experiment was conducted. In comparison to a freshly prepared sensor element, the sensor aged for a duration of 1 week under laboratory conditions showed the same characteristics because of the stability of polyaniline.

Sensor Response Selectivity. Proximity drop tests were conducted to check for other interfering commonplace volatile organic compounds (VOCs) such as acetone and ethanol as shown in Figures 6b and 6c, respectively, also present in traces in the oral breath of those who have recently imbibed alcohol and those who are diabetic, respectively.[62,63] Test results reveal that although we detected sensitivity toward the analytes, the signal was negligible compared to that of moisture. In contrast to the sensor response observed for humidity, we observe an increase in resistivity when either an acetone or ethanol drop is brought closer to the sensor element. This elucidates that the proton hopping mechanism is not at play while sensing these analytes and is valid only for atmospheric humidity. Testing settings and procedure can be found elsewhere (see the Supporting Information).

Sensing Mechanism. By embedding rGO within the PVDF structure, we observed better sensor characteristics in terms of both response time and current, confirming previous reports of Borini et al.[64] The current response originates from a charge transfer mechanism based on ionic conductance. As mentioned before, we believe that the underlying mechanism for sensing is to follow the Grotthuss method of proton hopping.[65] The adsorption is driven by intermolecular hydrogen bond formation followed by the completion of conduction channels throughout the surface for proton transport and, finally, quick desorption due to the hydrophobicity of the PVDF/rGO backbone. Out of the three phases of PANi, the emeraldine salt (ES) possesses partly positive and partly neutral charged polymeric backbone, which ultimately results in switch-like positions throughout its structure. Once the H_2O molecules have adsorbed onto the surface, the switches close instantaneously, which results in a current increase with rising %RH levels. This occurs due to the transient formation of H_3O^+ species. The proton is then transferred across to the next nitrogen atom, by what is characterized as a "hop". This hop or exchange occurs due to an interplay between polarity and hydrophilicity and is necessary for the transfer of electrons within the network of PANi as explained through nuclear magnetic resonance (NMR) studies performed by Nechtschein et al.[66] Moreover, Stejskal et al. have elaborated on the variable-range hopping (VRH) mechanism which is observed in polyaniline and other amorphous semiconductors.[67] During the proton free induction decay study of PANi, they observed two peaks corresponding to the protons in the rigid polymer and also the protons of water absorbed in the polymer network. They proposed that electron conduction in PANi is by removal of one electron from one reduced unit and transferring to the oxidized unit.[68] For this transfer of electron, a proton must be exchanged between $-(NH)^+-$ and H_2O forming H_3O^+ as

shown in Figure 1b,c. We have found rGO to play key roles in enhancing this conductance during the proton hop as previously discussed. Indeed, this two-pronged approach to increase ionic and electronic conductivity in our material has resulted in good selectivity at higher humidity levels. In the event that there are multiple conduction channels on the PANi surface, the proton hop occurs even via neighboring H_2O molecules, resulting in the formation of H_3O^+ and OH^- species as explained by Farahani et al.[69] To understand the effect of rGO within the fibers, PVDF was spun without rGO and with 4 mg of rGO. These fibers were coated with PANi via SILAR and examined for humidity response by a chronoamperometric study. The response of fibers without rGO is shown in Figure S6a. The current output under 90% RH of oral breath was 10 nA with a response time of 25 s. However, there was a stark increase (∼65%) in the current output in the presence of rGO (4 mg) and a decrease in response time to 7 s. This output along with the response time was further improved by doubling the concentration of rGO to 8 mg; the rise in current output was ∼1000 times, and the response time for sensing humidity reduced to ∼1 s. Additionally, a table comparing our sensor features with other reports is available in Table S1.

Sensor Portability. For personal use, the sensor was combined with a prototyping circuit board (Arduino) to perform the chronoamperometric study. Although the device can be powered externally by a small battery source (2 V), it was tethered to a laptop system via universal serial bus (USB) cable to acquire data. The chronoamperometric response collected in the presence of breath humidity is shown in Figure S7a. After a period of inactivity (100 s), breath cycles were suddenly initiated and continued for another 300 s to observe the response characteristics of the sensor. The current output rose to 0.8 mA as soon as the fibers were saturated with nasal breath. The increase in current output in the presence of rGO is appreciable in terms of response time. Because of increased current, the device may face higher power loads. Although not encountered while testing, future work involved reducing the bias voltage and reducing noise. The circuit diagram explaining the sensor element arrangement with Arduino is shown in Figure S7c. Further data refinement, in the form of long-term data acquisition, will provide a deeper understanding of various underlying patterns and parameters in our day-to-day breath cycles.

■ CONCLUSION AND OUTLOOK

The PANi-coated PVDF/rGO nanofibers have been shown to provide a robust response to humidity and can be calibrated to measure %RH levels from desiccated to saturated conditions (10−95% RH). Sensor characteristics reveal high sensitivity, especially under near-saturated conditions of 70−95% RH, confirming its viability for breath sensing. The sensor response can be sustained at higher current ranges (∼mA−μA). Moreover, based on materials optimization, small quantities of rGO (8 mg) can be used to fabricate up to 400 viable sensor elements, making it cost-effective on a large scale. A repeatable dynamic response has been recorded before and after physical activity which supports its use in health monitoring. In parallel, the device can replace most commercially available humidity sensors due to its superior characteristics and stability. We combined our sensing element with an Arduino module that can collect the chronoamperometric data, with the objective of using the device under lower operating voltages of <1 V.

Future work would involve collecting such breath data from multiple individuals for long spans of time, recognizing patterns, and tying the information to vital clinical conditions. The device may find applications in tracking calories burnt during exercise via breath rate and humidity levels, as well as in hospitals as low-cost and low-energy alternatives for patient monitoring.

■ ASSOCIATED CONTENT

Ⓢ Supporting Information

The Supporting Information is available free of charge on the ACS Publications website at DOI: 10.1021/acsaelm.9b00123.

> Materials and methods for preparing rGO; device fabrication methodology; Raman spectrum of PVDF/rGO composite; IR spectra of fibers; TEM of rGO and fiber composite; CV of PANi; breath analysis combined with a prototyping platform; water contact angle and sensor performance comparison between reported devices and present experiments (PDF)

■ AUTHOR INFORMATION

Corresponding Author

*E-mail pradeep@iitm.ac.in; Fax +91-44-2257-0545.

ORCID Ⓞ

Sourav Kanti Jana: 0000-0001-5772-7022

Thalappil Pradeep: 0000-0003-3174-534X

Author Contributions

S.A.I. and P.S. contributed equally to this work.

Notes

The authors declare no competing financial interest.

■ ACKNOWLEDGMENTS

■ REFERENCES

(1) Vanhoestenberghe, A.; Donaldson, N. Corrosion of Silicon Integrated Circuits and Lifetime Predictions in Implantable Electronic Devices. *J. Neural Eng.* **2013**, *10* (3), 031002.

(2) Paull, R. E. Effect of Temperature and Relative Humidity on Fresh Commodity Quality. *Postharvest Biol. Technol.* **1999**, *15* (3), 263−277.

(3) Nolte, A. J.; Treat, N. D.; Cohen, R. E.; Rubner, M. F. Effect of Relative Humidity on the Young ' s Modulus of Polyelectrolyte Multilayer Films and Related Nonionic Polymers. *Macromolecules* **2008**, *41*, 5793−5798.

(4) Rohde, F.; Normand, M. D.; Peleg, M. Effect of Equilibrium Relative Humidity on the Mechanical Signatures of Brittle Food Materials. *Biotechnol. Prog.* **1993**, *9* (5), 497−503.

(5) Tang, J. W. The Effect of Environmental Parameters on the Survival of Airborne Infectious Agents. *J. R. Soc., Interface* **2009**, *6*, 737−746.

(6) Zuo, Y. Y.; Gitiafroz, R.; Acosta, E.; Policova, Z.; Cox, P. N.; Hair, M. L.; Neumann, A. W. Effect of Humidity on the Adsorption

Kinetics of Lung Surfactant at Air-Water Interfaces. *Langmuir* **2005**, *21* (23), 10593−10601.

(7) Xu, P.; Kujundzic, E.; Peccia, J.; Schafer, M. P.; Moss, G.; Hernandez, M.; Miller, S. L. Impact of Environmental Factors on Efficacy of Upper-Room Air Ultraviolet Germicidal Irradiation for Inactivating Airborne Mycobacteria. *Environ. Sci. Technol.* **2005**, *39* (24), 9656−9664.

(8) Tatara, T.; Tsuzaki, K. An Apnea monitor using a rapid-response hygrometer. *J. Clin. Monit.* **1997**, *13*, 5−9.

(9) Oki, Y.; Kaneko, M.; Fujimoto, Y.; Sakai, H.; Misu, S.; Mitani, Y.; Yamaguchi, T.; Yasuda, H.; Ishikawa, A. Usefulness of the 6-minute Walk Test as a Screening Test for Pulmonary Arterial Enlargement in COPD. *Int. J. Chronic Obstruct. Pulm. Dis.* **2016**, *11* (1), 2869−2875.

(10) Hirsch, J. A.; Bishop, B. Respiratory Sinus Arrhythmia in Humans: How Breathing Pattern Modulates Heart Rate. *Am. J. Physiol.* **1981**, *241* (4), 620−629.

(11) Huang, Z.-M.; Zhang, Y.-Z.; Kotaki, M.; Ramakrishna, S. A Review on Polymer Nanofibers by Electrospinning and Their Applications in Nanocomposites. *Compos. Sci. Technol.* **2003**, *63* (15), 2223−2253.

(12) Chinnappan, A.; Baskar, C.; Baskar, S.; Ratheesh, G.; Ramakrishna, S. An Overview of Electrospun Nanofibers and Their Application in Energy Storage, Sensors and Wearable/Flexible Electronics. *J. Mater. Chem. C* **2017**, *5* (48), 12657−12673.

(13) Zhu, P.; Nair, A. S.; Shengjie, P.; Shengyuan, Y.; Ramakrishna, S. Facile Fabrication of TiO_2-Graphene Composite with Enhanced Photovoltaic and Photocatalytic Properties by Electrospinning. *ACS Appl. Mater. Interfaces* **2012**, *4* (2), 581−585.

(14) Binitha, G.; Soumya, M. S.; Madhavan, A. A.; Praveen, P.; Balakrishnan, A.; Subramanian, K. R. V.; Reddy, M. V.; Nair, S. V.; Nair, A. S.; Sivakumar, N. Electrospun α-Fe_2O_3 Nanostructures for Supercapacitor Applications. *J. Mater. Chem. A* **2013**, *1* (38), 11698−11704.

(15) Wang, X.; Sun, F.; Yin, G.; Wang, Y.; Liu, B.; Dong, M. Tactile-Sensing Based on Flexible PVDF Nanofibers via Electrospinning: A Review. *Sensors* **2018**, *18* (2), 330.

(16) Lee, H.; Wang, M.; Chen, P.; Gamelin, D. R.; Zakeeruddin, S. M.; Gratzel, M.; Nazeeruddin, M. K. Efficient CdSe Quantum Dot-Sensitized Solar Cells Prepared by an Improved Successive Ionic Layer Adsorption and Reaction Process. *Nano Lett.* **2009**, *9* (12), 4221−4227.

(17) Treml, B. E.; Savitzky, B. H.; Tirmzi, A. M.; Dasilva, J. C.; Kourkoutis, L. F.; Hanrath, T. Successive Ionic Layer Absorption and Reaction for Postassembly Control over Inorganic Interdot Bonds in Long-Range Ordered Nanocrystal Films. *ACS Appl. Mater. Interfaces* **2017**, *9* (15), 13500−13507.

(18) Navale, S. T.; Bandgar, D. K.; Chougule, M. A.; Patil, V. B. Facile Method of Preparation of PbS Films for NO_2 Detection. *RSC Adv.* **2015**, *5* (9), 6518−6527.

(19) Shishiyanu, S. T.; Shishiyanu, T. S.; Lupan, O. I. Sensing Characteristics of Tin-Doped ZnO Thin Films as NO_2 Gas Sensor. *Sens. Actuators, B* **2005**, *107* (1), 379−386.

(20) Esteves, C. H. A.; Iglesias, B. A.; Li, R. W. C.; Ogawa, T.; Araki, K.; Gruber, J. New Composite Porphyrin-Conductive Polymer Gas Sensors for Application in Electronic Noses. *Sens. Actuators, B* **2014**, *193*, 136−141.

(21) Najjar, R.; Nematdoust, S. A Resistive-Type Humidity Sensor Based on Polypyrrole and ZnO Nanoparticles: Hybrid Polymers Vis-a-Vis Nanocomposites. *RSC Adv.* **2016**, *6* (113), 112129−112139.

(22) Guo, Y. N.; Gao, Z. Y.; Wang, X. X.; Sun, L.; Yan, X.; Yan, S. Y.; Long, Y. Z.; Han, W. P. A Highly Stretchable Humidity Sensor Based on Spandex Covered Yarns and Nanostructured Polyaniline. *RSC Adv.* **2018**, *8* (2), 1078−1082.

(23) Zhang, D.; Wang, D.; Li, P.; Zhou, X.; Zong, X.; Dong, G. Facile Fabrication of High-Performance QCM Humidity Sensor Based on Layer-by-Layer Self-Assembled Polyaniline/Graphene Oxide Nanocomposite Film. *Sens. Actuators, B* **2018**, *255*, 1869−1877.

(24) Parvatikar, N.; Jain, S.; Khasim, S.; Revansiddappa, M.; Bhoraskar, S. V.; Prasad, M. V. N. A. Electrical and Humidity Sensing Properties of Polyaniline/WO 3 Composites. *Sens. Actuators, B* **2006**, *114* (2), 599−603.

(25) Li, X. Z.; Liu, S. R.; Guo, Y. Polyaniline-Intercalated Layered Double Hydroxides: Synthesis and Properties for Humidity Sensing. *RSC Adv.* **2016**, *6* (68), 63099−63106.

(26) Dhawale, D. S.; Salunkhe, R. R.; Jamadade, V. S.; Dubal, D. P.; Pawar, S. M.; Lokhande, C. D. Hydrophilic Polyaniline Nanofibrous Architecture Using Electrosynthesis Method for Supercapacitor Application. *Curr. Appl. Phys.* **2010**, *10* (3), 904−909.

(27) Zhong, W.; Chen, X.; Liu, S.; Wang, Y.; Yang, W. Synthesis of Highly Hydrophilic Polyaniline Nanowires and Sub-Micro/Nano-structured Dendrites on Poly(Propylene) Film Surfaces. *Macromol. Rapid Commun.* **2006**, *27* (7), 563−569.

(28) Feng, C.; Khulbe, K. C.; Matsuura, T.; Tabe, S.; Ismail, A. F. Preparation and Characterization of Electro-Spun Nanofiber Membranes and Their Possible Applications in Water Treatment. *Sep. Purif. Technol.* **2013**, *102*, 118−135.

(29) Wang, S.; Zhao, X.; Yin, X.; Yu, J.; Ding, B. Electret Polyvinylidene Fluoride Nanofibers Hybridized by Polytetrafluoroethylene Nanoparticles for High-Efficiency Air Filtration. *ACS Appl. Mater. Interfaces* **2016**, *8* (36), 23985−23994.

(30) Wang, L.-Y.; Yong, W. F.; Yu, L. E.; Chung, T.-S. Design of High Efficiency PVDF-PEG Hollow Fibers for Air Filtration of Ultrafine Particles. *J. Membr. Sci.* **2017**, *535*, 342−349.

(31) Laroche, G.; Marois, Y.; Guidoin, R.; King, M. W.; Martin, L.; How, T.; Douville, Y. Polyvinylidene Fluoride (PVDF) as a Biomaterial: From Polymeric Raw Material to Monofilament Vascular Suture. *J. Biomed. Mater. Res.* **1995**, *29* (12), 1525−1536.

(32) Zhang, S.; Cao, J.; Ma, N.; You, M.; Wang, X.; Meng, J. Fast and Facile Fabrication of Antifouling and Hemocompatible PVDF Membrane Tethered with Amino-Acid Modified PEG Film. *Appl. Surf. Sci.* **2018**, *428*, 41−53.

(33) Al Halabi, F.; Gryshkov, O.; Kuhn, A. I.; Kapralova, V. M.; Glasmacher, B. Force Induced Piezoelectric Effect of Polyvinylidene Fluoride and Polyvinylidene Fluoride-Co-Trifluoroethylene Nanofibrous Scaffolds. *Int. J. Artif. Organs* **2018**, *41* (11), 811−822.

(34) Kuang, Q.; Lao, C.; Wang, Z. L.; Xie, Z.; Zheng, L. High-Sensitivity Humidity Sensor Based on a Single SnO 2 Nanowire. *J. Am. Chem. Soc.* **2007**, *129* (19), 6070−6071.

(35) Wang, Z.; Xiao, Y.; Cui, X.; Cheng, P.; Wang, B.; Gao, Y.; Li, X.; Yang, T.; Zhang, T.; Lu, G. Humidity-Sensing Properties of Urchinlike CuO Nanostructures Modified by Reduced Graphene Oxide. *ACS Appl. Mater. Interfaces* **2014**, *6* (6), 3888−3895.

(36) Sreedhara, M. B.; Ghatak, J.; Bharath, B.; Rao, C. N. R. Atomic Layer Deposition of Ultrathin Crystalline Epitaxial Films of V2O5. *ACS Appl. Mater. Interfaces* **2017**, *9* (3), 3178−3185.

(37) Zhao, H.; Zhang, T.; Qi, R.; Dai, J.; Liu, S.; Fei, T. Drawn on Paper: A Reproducible Humidity Sensitive Device by Handwriting. *ACS Appl. Mater. Interfaces* **2017**, *9* (33), 28002−28009.

(38) Zhen, Z.; Li, Z.; Zhao, X.; Zhong, Y.; Zhang, L.; Chen, Q.; Yang, T.; Zhu, H. Formation of Uniform Water Microdroplets on Wrinkled Graphene for Ultrafast Humidity Sensing. *Small* **2018**, *14* (15), 1703848.

(39) Güder, F.; Ainla, A.; Redston, J.; Mosadegh, B.; Glavan, A.; Martin, T. J.; Whitesides, G. M. Paper-Based Electrical Respiration Sensor. *Angew. Chem., Int. Ed.* **2016**, *55* (19), 5727−5732.

(40) Zhang, Y.; Yu, K.; Jiang, D.; Zhu, Z.; Geng, H.; Luo, L. Zinc Oxide Nanorod and Nanowire for Humidity Sensor. *Appl. Surf. Sci.* **2005**, *242* (1−2), 212−217.

(41) Chen, Z.; Lu, C. Humidity Sensors: A Review of Materials and Mechanisms. *Sens. Lett.* **2005**, *3* (4), 274−295.

(42) Chen, M.; Zhang, C.; Li, L.; Liu, Y.; Li, X.; Xu, X.; Xia, F.; Wang, W.; Gao, J. Sn Powder as Reducing Agents and SnO₂ Precursors for the Synthesis of SnO₂-Reduced Graphene Oxide Hybrid Nanoparticles. *ACS Appl. Mater. Interfaces* **2013**, *5* (24), 13333−13339.

(43) Buvailo, A. I.; Xing, Y.; Hines, J.; Dollahon, N.; Borguet, E. TiO₂/LiCl-Based Nanostructured Thin Film for Humidity Sensor Applications. *ACS Appl. Mater. Interfaces* **2011**, *3* (2), 528−533.

(44) He, J.; Xiao, P.; Shi, J.; Liang, Y.; Lu, W.; Chen, Y.; Wang, W.; Théato, P.; Kuo, S. W.; Chen, T. High Performance Humidity Fluctuation Sensor for Wearable Devices via a Bioinspired Atomic-Precise Tunable Graphene-Polymer Heterogeneous Sensing Junction. *Chem. Mater.* **2018**, *30* (13), 4343−4354.

(45) Mogera, U.; Sagade, A. A.; George, S. J.; Kulkarni, G. U. Ultrafast Response Humidity Sensor Using Supramolecular Nanofibre and Its Application in Monitoring Breath Humidity and Flow. *Sci. Rep.* **2015**, *4*, 1−9.

(46) Tan, Y.; Fang, L.; Xiao, J.; Song, Y.; Zheng, Q. Grafting of Copolymers onto Graphene by Miniemulsion Polymerization for Conductive Polymer Composites: Improved Electrical Conductivity and Compatibility Induced by Interfacial Distribution of Graphene. *Polym. Chem.* **2013**, *4* (10), 2939−2944.

(47) Yuan, B.; Wang, B.; Hu, Y.; Mu, X.; Hong, N.; Liew, K. M.; Hu, Y. Electrical Conductive and Graphitizable Polymer Nanofibers Grafted on Graphene Nanosheets: Improving Electrical Conductivity and Flame Retardancy of Polypropylene. *Composites, Part A* **2016**, *84*, 76−86.

(48) Kano, S.; Dobashi, Y.; Fujii, M. Silica Nanoparticle-Based Portable Respiration Sensor for Analysis of Respiration Rate, Pattern, and Phase During Exercise. *IEEE Sensors Lett.* **2018**, *2* (1), 1−4.

(49) Watanabe, A.; Mori, K.; Iwasaki, Y.; Nakamura, Y.; Niizuma, S. Electrochromism of Polyaniline Film Prepared by Electrochemical Polymerization. *Macromolecules* **1987**, *20* (8), 1793−1796.

(50) Planes, G. A.; Rodríguez, J. L.; Miras, M. C.; García, G.; Pastor, E.; Barbero, C. A. Spectroscopic Evidence for Intermediate Species Formed during Aniline Polymerization and Polyaniline Degradation. *Phys. Chem. Chem. Phys.* **2010**, *12* (35), 10584−10593.

(51) Gu, S.; He, G.; Wu, X.; Hu, Z.; Wang, L.; Xiao, G.; Peng, L. Preparation and Characterization of Poly(Vinylidene Fluoride)/Sulfonated Poly(Phthalazinone Ether Sulfone Ketone) Blends for Proton Exchange Membrane. *J. Appl. Polym. Sci.* **2009**, *116* (2), 852−860.

(52) Trchová, M.; Stejskal, J. Polyaniline: The Infrared Spectroscopy of Conducting Polymer Nanotubes (IUPAC Technical Report). *Pure Appl. Chem.* **2011**, *83* (10), 1803−1817.

(53) Constantino, C. J. L.; Job, A. E.; Simões, R. D.; Giacometti, J. A.; Zucolotto, V.; Oliveira, O. N.; Gozzi, G.; Chinaglia, D. L. Phase Transition in Poly(Vinylidene Fluoride) Investigated with Micro-Raman Spectroscopy. *Appl. Spectrosc.* **2005**, *59* (3), 275−279.

(54) Zheng, J.; He, A.; Li, J.; Han, C. C. Polymorphism Control of Poly(Vinylidene Fluoride) through Electrospinning. *Macromol. Rapid Commun.* **2007**, *28* (22), 2159−2162.

(55) Furukawa, T. Ferroelectric Properties of Vinylidene Fluoride Copolymers. *Phase Transitions* **1989**, *18* (3−4), 143−211.

(56) Grzeszczuk, M.; Grańska, A.; Szostak, R. Raman Spectroelectrochemistry of Polyaniline Synthesized Using Different Electrolytic Regimes-Multivariate Analysis. *Int. J. Electrochem. Sci.* **2013**, *8* (7), 8951−8965.

(57) Evans, J. C. The Vibrational Assignments and Configuration of Aniline, Aniline-NHD and Aniline-ND2. *Spectrochim. Acta* **1960**, *16* (4), 428−442.

(58) Sun, Q. The Raman OH Stretching Bands of Liquid Water. *Vib. Spectrosc.* **2009**, *51* (2), 213−217.

(59) Choe, C.; Lademann, J.; Darvin, M. E. Depth Profiles of Hydrogen Bound Water Molecule Types and Their Relation to Lipid and Protein Interaction in the Human Stratum Corneum in Vivo. *Analyst* **2016**, *141* (22), 6329−6337.

(60) Peng, G.; Tisch, U.; Adams, O.; Hakim, M.; Shehada, N.; Broza, Y. Y.; Billan, S.; Abdah-Bortnyak, R.; Kuten, A.; Haick, H. Diagnosing Lung Cancer in Exhaled Breath Using Gold Nanoparticles. *Nat. Nanotechnol.* **2009**, *4* (10), 669−673.

(61) Grubin, D.; Madsen, L. Lie Detection and the Polygraph: A Historical Review. *J. Forensic Psychiatry Psychol.* **2005**, *16* (2), 357−369.

(62) Wu, L.; McIntosh, M.; Zhang, X.; Ju, H. Amperometric Sensor for Ethanol Based on One-Step Electropolymerization of Thionine-Carbon Nanofiber Nanocomposite Containing Alcohol Oxidase. *Talanta* **2007**, *74* (3), 387−392.

(63) Choi, S. J.; Lee, I.; Jang, B. H.; Youn, D. Y.; Ryu, W. H.; Park, C. O.; Kim, I. D. Selective Diagnosis of Diabetes Using Pt-Functionalized WO3 Hemitube Networks as a Sensing Layer of Acetone in Exhaled Breath. *Anal. Chem.* **2013**, *85* (3), 1792−1796.

(64) Borini, S.; White, R.; Wei, D.; Astley, M.; Haque, S.; Spigone, E.; Harris, N.; Kivioja, J.; Ryhänen, T. Ultrafast Graphene Oxide Humidity Sensors. *ACS Nano* **2013**, *7* (12), 11166−11173.

(65) Farahani, H.; Wagiran, R.; Hamidon, M. N. Humidity Sensors Principle, Mechanism, and Fabrication Technologies: A Comprehensive Review. *Sensors* **2014**, *14*, 7881−7939.

(66) Nechtschein, M.; Santier, C. NMR Observation of Proton Exchange in the Conducting Polymer Polyaniline. *J. Phys. (Paris)* **1986**, *47* (6), 935−937.

(67) Stejskal, J.; Trchová, M.; Bober, P.; Humpolíček, P.; Kašpárková, V.; Sapurina, I.; Shishov, M. A.; Varga, M. Conducting Polymers: Polyaniline. *Encyclopedia of Polymer Science and Technology*, 2015; p 1.

(68) Travers, J.; Nechtschein, M. Water Effects in Polyaniline: A New Conduction Process. *Synth. Met.* **1987**, *21* (1−3), 135−141.

(69) Doan, T. C. D.; Ramaneti, R.; Baggerman, J.; Tong, H. D.; Marcelis, A. T. M.; Van Rijn, C. J. M. Intrinsic and Ionic Conduction in Humidity-Sensitive Sulfonated Polyaniline. *Electrochim. Acta* **2014**, *127*, 106−114.